PAPER

Check for updates

Preparation of a reduced graphene oxide/SiO₂/Fe₃O₄ UV-curing material and its excellent microwave absorption properties

Yingjie Xu,[ab] Qi Wang,[a] Yunfeng Cao, [ID] *[a] Xianfu Wei[b] and Beiqing Huang[b]

A RGO/SiO₂/Fe₃O₄ UV-curing material was synthesized and its nanostructures and morphologies were characterized at the nanoscale. Microwave absorption properties show that the RGO/SiO₂/Fe₃O₄ hybrid has enhanced electromagnetic wave absorption characteristics. The maximum reflection loss of the RGO/SiO₂/Fe₃O₄ UV-curing material reaches −56.4 dB at 8.1 GHz with the thickness of 4.5 mm, and the maximum effective absorption bandwidth reaches 7.1 GHz with the thickness of 3.0 mm. Investigations reveal that the dispersion and reflection loss of Fe₃O₄ which is wrapped by SiO₂ is obviously improved. The enhanced absorption properties of the RGO/SiO₂/Fe₃O₄ hybrid are ascribed to the synergistic effect of magnetic Fe₃O₄ nanocrystals and light-weight graphene. These results suggest that the RGO/SiO₂/Fe₃O₄ hybrid could be used as a kind of candidate absorber. The mass ratio of the RGO/SiO₂/Fe₃O₄ to UV-curing material was only 0.2%. It is believed that such a composite will find its wide applications in a microwave absorbing area.

Introduction

With the rapid development of electronic instruments and telecommunication technologies, the phenomena of electromagnetic interference and electromagnetic compatibility have become more and more serious problems. The accompanying electromagnetic pollution can not only interrupt the operation of electronic devices but is also harmful to human health. Therefore microwave absorption materials play important roles in civilian and military applications.[1–3] Microwave absorption materials with a strong absorption value, wide absorption frequency, thin matching thickness and lightweight characteristics are urgently required. Much effort has been focused on the fabrication of microwave absorption materials, such as ferrites, magnetic metals, dielectrics and so on.[4,5] Among the magnetic components, Fe₃O₄ nanostructures have attracted extensive interest as microwave absorbers because of their unique properties, such as moderate saturation magnetization value, high Curie temperature. However, the large density and high matching thickness of these materials greatly restrict their technical applications.[6–10] The exploration of highly efficient and lightweight microwave absorption materials with thin thickness is still a big challenge. Compared with traditional ferrite materials, carbon materials have advantages of high dielectric loss and low density.[11–14] Carbon microwave

absorption materials mainly include carbon nanocapsules, carbon nanotubes, carbon fibers, carbon foam and graphene.[15] Compared with other carbon materials, graphene has more prominent intrinsic physical and chemical properties, including superior electronic, thermal and mechanical properties as well as its chemical stability.[15–17] Graphene oxide (GO) and reduced graphene oxide (RGO), as important derivatives of graphene, have realized production in large scale, owing to the production scalability and convenient process. GO and RGO have numerous oxygen-containing groups (epoxides, alcohols, and carboxylic acid groups) or defects on the surface while maintaining the same 2D planar structure like pristine graphene.[18,19] These functional groups make GO and RGO ideal candidates to act as nanoscale building blocks for incorporation into novel functional hybrids. However, the reflection loss of GO and RGO is poor, which is unsuitable for practical applications.[20–22] In particular, taking advantage of the combined benefits of magnetic nanocrystals and reduced graphene oxide, magnetic nanocrystals/reduced graphene hybrids show great potential as novel light-weight electromagnetic absorption materials. The synergistic interaction effect between the magnetic nanocrystals and graphene may result in better absorption characteristics.[23–25] The thermal energy converted by the absorbed electromagnetic wave can spread rapidly due to the remarkable thermal conductivity of graphene nanosheets. Previous reports demonstrate that combination of GO with Fe₃O₄ nanoparticles would enhance its microwave absorbing properties.[2–4,26–29] Graphene-supported composites usually have a problem of poor dispersion, which greatly hinders the further design of porous structures.[30–42] The magnetic nanocrystals/

a College of Light Industry Science and Engineering, Nanjing Forestry University, Longpan Rd, No. 159, Nanjing, 210037, PR China. E-mail: yunfcao@163.com

b Beijing Institute of Graphic Communication, Xinghua North Rd, No. 25, Beijing, 102600, PR China

reduced graphene hybrids employed in the above studies were usually hydrophilic or easily oxidized, which restricts their potential applications in some specific environments like humid climates.[43–47] The synthesis of RGO/SiO$_2$/Fe$_3$O$_4$ composite is a newly-developed method, which is more facile to design microstructure materials without sacrificing the contact between graphene and the other materials. The core–shell structural of Fe$_3$O$_4$/SiO$_2$ nanocomposite can improve the dispersion and stability of Fe$_3$O$_4$.

Due to its ability to produce microstructure patterns on large area substrates with high throughput, UV curing technique is a promising technology for microwave absorption materials.[48–50] However, for it to become a technology for the mass production of microwave absorption materials, we must first prepare UV-curing material.

Herein, we report the preparation of RGO/SiO$_2$/Fe$_3$O$_4$ UV-curing material with improved microwave absorbing capability. Firstly the core–shell structural Fe$_3$O$_4$/SiO$_2$ nanocomposite particles were prepared to improve the dispersion and stability of Fe$_3$O$_4$. Moreover we synthesized the RGO/SiO$_2$/Fe$_3$O$_4$ composite which is blended with UV cured resin to prepare RGO/SiO$_2$/Fe$_3$O$_4$ UV-curing material. The morphology and structure of as-prepared composite were investigated. The cured composite exhibits excellent microwave absorption performances.

Experimental

Synthesis of Fe$_3$O$_4$/SiO$_2$ composite nano-particles

FeCl$_3$·6H$_2$O (2.7 g) was dissolved in ethylene glycol (80 mL) to form a clear solution, followed by the addition of NaAc (7.2 g) and polyethylene glycol (2.0 g). The mixture was stirred vigorously for 30 min and then sealed in a Teflon-lined stainless-steel autoclave (100 mL capacity). The autoclave was heated to and maintained at 200 °C for 8 h, and allowed to cool to room temperature. The black products were washed several times with alcohol and water, then dried at 60 °C for 12 h. Fe$_3$O$_4$ nano-particles as-prepared (0.1 g) were dissolved in alcohol (50 mL) by ultrasonic dispersion process for 30 min, followed by the addition of H$_2$O (0.25 g) and NH$_3$·H$_2$O (0.15 g). The mixture was stirred for 10 min at 40 °C, then TEOS (250 μL) is cautiously added dropwise and keep stirring for 2 h. The products were washed several times with alcohol and dried at 60 °C for 12 h.

Preparation of RGO/SiO$_2$/Fe$_3$O$_4$ UV-curing material

RGO/SiO$_2$/Fe$_3$O$_4$ composite was synthesis by a condensation reaction. Fe$_3$O$_4$/SiO$_2$ nano-particles (30 mg) were dissolved in ethylene glycol (15 mL) by ultrasonic dispersion process for 2 h, followed by the addition of KH550 (10 μL). The mixture was stirred for 2 h at 78 °C. The ethylene glycol solution of aminated Fe$_3$O$_4$/SiO$_2$ is prepared. GO (70 mg) was dissolved in water (20 mL) by ultrasonic dispersion process for 2 h, which was prepared by Hummer's method,[51] followed by the addition of EDC. HCL (48 mg) and NHS (57 mg), the mixture was stirred for 20 min at room temperature. Then the ethylene glycol solution of aminated Fe$_3$O$_4$/SiO$_2$ (15 mL) was added in and stirred for

24 h at room temperature. The mixture was prepared into ethylene glycol solution of RGO/SiO$_2$/Fe$_3$O$_4$ by rotary evaporation and vacuum drying at 60 °C for 12 h.

The ethylene glycol solution of RGO/SiO$_2$/Fe$_3$O$_4$ (0.4 g) was added to UV curable polyurethane (EBECRYL 151, Allnex, American) (0.6 g) and methyl benzoylformate (0.16 g), the mixture was stirred for 30 min at room temperature. The mass ratio of RGO/SiO$_2$/Fe$_3$O$_4$ in the UV-curing material approximates at 0.2%. Preparation of GO, Fe$_3$O$_4$ and Fe$_3$O$_4$/SiO$_2$ UV-curing material at the same mass ratio.

Characterization

The morphology and of the composite was examined by transmission electron microscopy (TEM; G2 F20, FEI-Tecnai, 200 kV, Hillsboro, USA). X-ray diffraction (XRD), system at 40 kV and 100 mA of Cu Kα (Ultima IV, Rigaku, Japan). Raman spectra were obtained on a Renishaw Ramascope (confocal spectrometer with 633 nm laser, inVia, Renishaw, Gloucester-shire, U.K.), electromagnetic parameters were measured by a vector network analyzer (VNA, N5234A PAN-L, Agilent, USA) in the range of 2–18 GHz, in which the RGO/SiO$_2$/Fe$_3$O$_4$ UV-curing material, were cured to be toroidal samples (outer diameter: 7 mm, inner diameter: 3.04 mm, and thickness: 3 mm).

Results and discussion

Microstructure of RGO/SiO$_2$/Fe$_3$O$_4$ composite

Fig. 2 shows the XRD patterns of GO, Fe$_3$O$_4$ and RGO/SiO$_2$/Fe$_3$O$_4$. The XRD pattern of the GO (Fig. 1a) shows a sharp peak at $2\theta = 11.8°$, corresponding to the (001) reflection of GO. The XRD pattern of the RGO/SiO$_2$/Fe$_3$O$_4$ (Fig. 1c) shows peaks at 30.3, 35.7, 43.4, 53.7, 57.1 and 62.8 are observed, which are very similar to that of the pure Fe$_3$O$_4$ (Fig. 1b), and could be indexed as the characteristic (220), (311), (400), (422), (511) and (440) reflections of the pure cubic spinel crystal structure of Fe$_3$O$_4$ (JCPDS no. 19-0629), the broad peak at 23.2° can be attributed to the graphite-like structure (002), suggesting that most of oxygen functionalities are removed.

In order to understand the chemical bonding and structural changes of the carbon framework in RGO/SiO$_2$/Fe$_3$O$_4$ hybrids and GO, Raman spectroscopy techniques was adopted. Fig. 3 shows two representative Raman spectra of the GO and RGO/SiO$_2$/Fe$_3$O$_4$ hybrid. Two characteristic peaks are observed at ~1331 cm^{-1} and ~1593 cm^{-1}, which correspond to the D and G bands respectively.[52,53] The G band is attributed to the first-
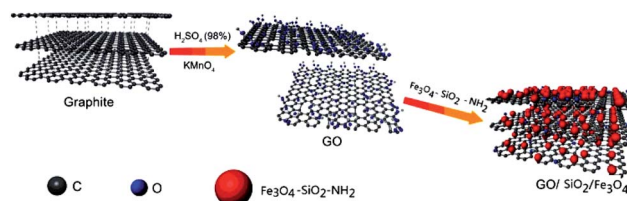

Fig. 1 Schematic illustration of the formation process of RGO/SiO$_2$/Fe$_3$O$_4$ composite.
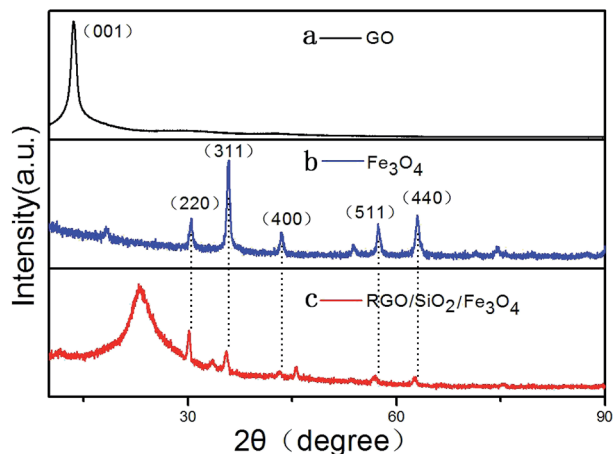
Fig. 2 XRD spectra of GO, Fe_3O_4, and $RGO/SiO_2/Fe_3O_4$.

order scattering of the E_{2g} vibration mode, which corresponds to the in-plane vibration of sp^2 carbon domains in the hexagonal lattice of graphene nanosheets. The D band is associated with the K-point phonons of the A_{1g} mode, which is due to the vibration of sp^3 carbon domains in the plane terminations of disordered graphite. The intensity ratio of D and G bands (I_D/I_G) is related to the disordered structure of carbon.[54–57] Compared with GO, the $RGO/SiO_2/Fe_3O_4$ hybrids reveal an obviously enhanced value of I_D/I_G, suggesting that the presence of more numerous but smaller sp^2 carbon domain resulted from the reduction process of GO during the formation of $RGO/SiO_2/Fe_3O_4$ hybrids.

The morphologies and structures of Fe_3O_4, Fe_3O_4/SiO_2 and $RGO/SiO_2/Fe_3O_4$ composite were investigated by TEM. Fig. 4a shows the TEM image of Fe_3O_4 nanoparticles, in which we can see that the dispersion of Fe_3O_4 is poor. Fig. 4b shows the TEM image of Fe_3O_4/SiO_2, the dispersion of Fe_3O_4 is significantly improved by SiO_2. Fig. 4c presents a magnification TEM image of the Fe_3O_4/SiO_2 composites, it can be seen that the Fe_3O_4 spheres are entirely wrapped by SiO_2, which has the porous structure. As seen from the low magnification TEM images of $RGO/SiO_2/Fe_3O_4$ composite (Fig. 4d and e), the graphene

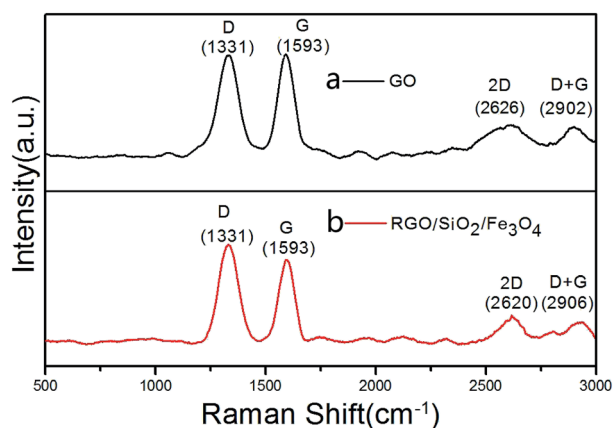Fig. 4 TEM images of the Fe_3O_4 (a), Fe_3O_4/SiO_2 composite nanoparticles (b and c), $RGO/SiO_2/Fe_3O_4$ composite (d and e) and a HRTEM image and SAED pattern of the $RGO/SiO_2/Fe_3O_4$ composite (f).

nanosheets are well coated by Fe_3O_4 nanoparticles with diameters from 20 nm to 30 nm, which has a good dispersion. Moreover, almost no Fe_3O_4 nanoparticles are found outside of the GO nanosheets, indicating that condensation reaction synthesis of $RGO/SiO_2/Fe_3O_4$ composite is high efficiency. HRTEM image of particles (Fig. 4f) reveals that Fe_3O_4 nanoparticles are monocrystalline,[58] the interplanar spacings between the lattice fringes are 0.484 nm (111) and 0.258 nm (311).

Dielectric and EM wave absorption properties

Fig. 5 shows the real (ε') and imaginary (ε'') parts of the permittivity, the real (μ') and imaginary (μ'') parts of the permeability and the tangent loss of the samples. As shown in Fig. 5a, the ε' of the samples decrease with increasing the frequency in the range of 2–18 GHz, demonstrating a frequency-dependent dielectric response, the value of $RGO/SiO_2/Fe_3O_4$ is higher than others. The ε'' of Fe_3O_4 and Fe_3O_4/SiO_2 (Fig. 5b) decrease approximately linearly with increasing the frequency in the range of 2–18 GHz; the ε'' of GO and $RGO/SiO_2/Fe_3O_4$ remain almost unchanged as the frequency increases, and their

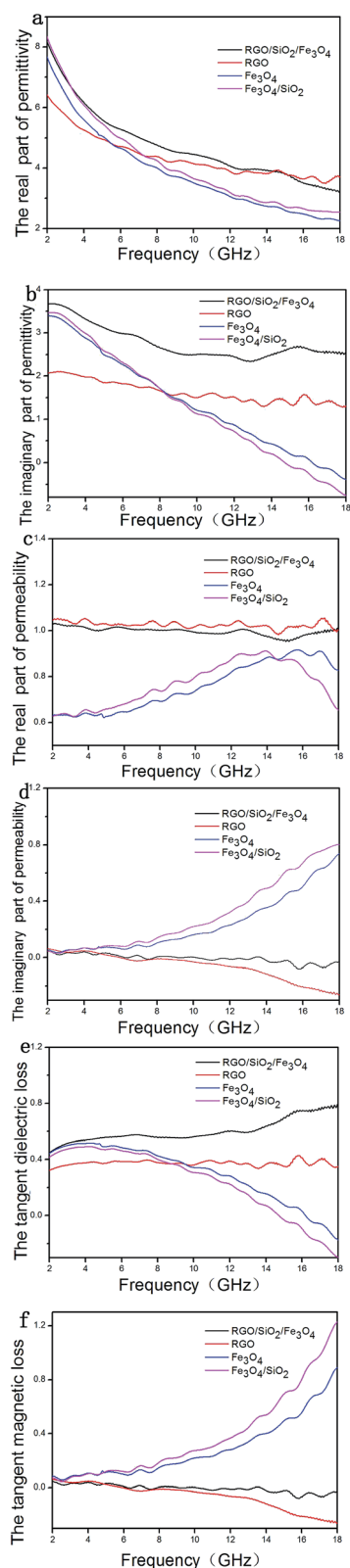Fig. 3 Raman spectra of GO, $RGO/SiO_2/Fe_3O_4$.

Fig. 5 The (a) real part (b) imaginary part of permittivity; the (c) real part (d) imaginary part of permeability; the tangent (e) dielectric and (f) magnetic loss as a function of frequency for the samples.
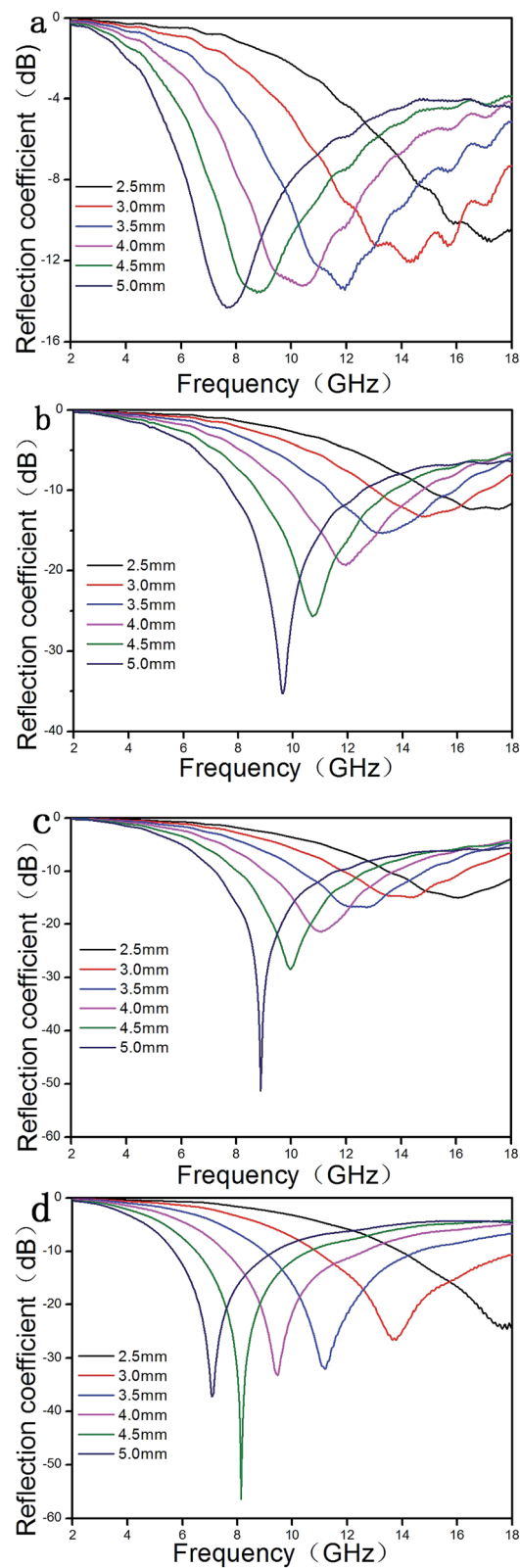

Fig. 6 Reflection coefficient calculated for the samples at different thicknesses.

average value were 1.64 and 2.79; the value of RGO/SiO$_2$/Fe$_3$O$_4$ is higher than others. The μ' of Fe$_3$O$_4$ (Fig. 5c) increases in the range of 2 to 15.7 GHz then decline, which has a peak value of 0.92; the μ' of Fe$_3$O$_4$/SiO$_2$ increases in the range of 2 to 13.95 GHz then decline, which has a peak value of 0.92; the μ' of GO and RGO/SiO$_2$/Fe$_3$O$_4$ remain almost unchanged as the frequency increases, and their average value were 1.03 and 1. The μ'' of Fe$_3$O$_4$ and Fe$_3$O$_4$/SiO$_2$ (Fig. 5d) increases in the range of 2–18; the value of GO and RGO/SiO$_2$/Fe$_3$O$_4$ approximate to 0.1 and the value of RGO/SiO$_2$/Fe$_3$O$_4$ is higher then GO. The tangent dielectric loss of Fe$_3$O$_4$ and Fe$_3$O$_4$/SiO$_2$ (Fig. 5e) decrease with increasing the frequency in the range of 2–18 GHz; the tangent dielectric loss of GO and RGO/SiO$_2$/Fe$_3$O$_4$ remain almost unchanged as the frequency increases, and their average value were 0.36 and 0.57. The tangent magnetic loss of Fe$_3$O$_4$ and Fe$_3$O$_4$/SiO$_2$ increase in the range of 2–18 GHz; the values of GO and RGO/SiO$_2$/Fe$_3$O$_4$ approximate to 0.1 and the value of RGO/SiO$_2$/Fe$_3$O$_4$ is higher then GO.

According to the transmit-line theory, the reflection loss (R) can be calculated by the following equations:

$$RL\ (dB) = 20\ \log|(Z_{in} - 1)/(Z_{in} + 1)| \tag{1}$$

$$Z_{in} = Z_0(\mu_\gamma/\varepsilon_\gamma)^{1/2}\ \tanh[j(2\pi fd/c)(\mu_\gamma\varepsilon_\gamma)^{1/2}] \tag{2}$$

when Z_{in} is the input impedance of the absorber, Z_0 is the impedance of air, μ_γ and ε_γ are respectively the relative complex permeability and permittivity, f is the frequency of microwaves, d is the thickness of the absorber, and c is the velocity of electromagnetic waves in free space.[59]

The theoretical RC calculated for samples with different thickness.

As shown in Fig. 6a, the maximum reflection loss of GO is only −14.3 at 7.7 GHz for a layer of 5 mm thickness; the maximum reflection loss of Fe$_3$O$_4$ (Fig. 6b) is −35.3 at 9.6 GHz for a layer of 5 mm thickness; the maximum reflection loss of Fe$_3$O$_4$/SiO$_2$ (Fig. 6c) is −51.3 at 8.9 GHz for a layer of 5 mm thickness. The maximum reflection loss of Fe$_3$O$_4$/SiO$_2$ is significantly higher than Fe$_3$O$_4$.

The maximum reflection loss of RGO/SiO$_2$/Fe$_3$O$_4$ (Fig. 6d) reaches −56.4 dB at 8.1 GHz and the bandwidth corresponding to reflection less than −10 dB (90% absorption)[60] can reach 4.1 GHz (from 6.5 to 10.6 GHz) for a layer of 4.5 mm thickness. In addition, the bandwidth corresponding reflection loss of RGO/SiO$_2$/Fe$_3$O$_4$ less than −10 dB can reach 7.1 GHz (from 10.9 to 18 GHz) for a layer of 3.0 mm thickness. The results demonstrate that the RGO/SiO$_2$/Fe$_3$O$_4$ UV-curing materials have a large reflection loss and a wide absorption band.[61,62]

Conclusions

In summary, the RGO/SiO$_2$/Fe$_3$O$_4$ UV-curing material was synthesized and its nanostructures and morphologies were characterized at nanoscale. Microwave absorption properties show that the RGO/SiO$_2$/Fe$_3$O$_4$ hybrid has enhanced electromagnetic wave absorption characteristics. The maximum reflection loss of RGO/SiO$_2$/Fe$_3$O$_4$ UV-curing material reaches −56.4 dB at 8.1 GHz with the thickness of 4.5 mm, and the maximum effective absorption bandwidth reaches 7.1 GHz with the thickness of 3.0 mm. Investigations reveal that the dispersion and reflection loss of Fe$_3$O$_4$ which wrapped by SiO$_2$ is obviously improved. Moreover, the core–shell structural Fe$_3$O$_4$/SiO$_2$ nanocomposite particles are believed to be more stable and suitable to be applied in some particular environmental conditions. The enhanced absorption properties of the RGO/SiO$_2$/Fe$_3$O$_4$ hybrids are ascribed to the synergistic effect of magnetic Fe$_3$O$_4$ nanocrystal and light-weight graphene, including magnetic loss from magnetic Fe$_3$O$_4$ nanocrystals, dielectric loss from light-weight graphene. These results suggest that the RGO/SiO$_2$/Fe$_3$O$_4$ composite could be used as a kind of candidate absorber. The mass ratio of the RGO/SiO$_2$/Fe$_3$O$_4$ to UV-curing material was only 0.2%. It is believed that such composite will find its wide applications in microwave absorbing area.

Notes and references

1 X. H. Li, J. Feng, H. Zhu, C. H. Qu, J. T. Bai and X. l. Zheng, *RSC Adv.*, 2014, **4**, 33619–33625.
2 X. l. Zheng, J. Feng, Y. Zong, H. Miao, X. Y. Hu, J. T. Bai and X. H. Li, *J. Mater. Chem. C*, 2015, **3**, 4452–4463.
3 Z. X. Li, X. H. Li, Y. Zong, G. G. Tan, Y. Sun, Y. Y. Lan, M. He, Z. Y. Ren and X. L. Zheng, *Carbon*, 2017, **115**, 493–502.
4 X. h. Li, H. B. Yi, J. W. Zhang, J. Feng, F. S. Li, D. S. Xue, H. L. Zhang, Y. Peng and N. J. Mellors, *J. Nanopart. Res.*, 2013, **15**, 1472.
5 J. Feng, F. Z. Pu, Z. X. Li, X. H. Li, X. Y. Hu and J. T. Bai, *Carbon*, 2016, **104**, 214–225.
6 M. K. Han, X. W. Yin, L. Kong, M. Li, W. Y. Duan, L. T. Zhang and L. F. Cheng, *J. Mater. Chem. A*, 2014, **2**, 16403–16409.
7 P. B. Liu, Y. Huang, L. Wang and W. Zhang, *J. Alloys Compd.*, 2013, **573**, 151–156.
8 H. X. Pan, X. W. Yin, J. M. Xue, L. F. Cheng and L. T. Zhang, *Carbon*, 2016, **107**, 36–45.
9 P. B. Liu, Y. Huang, L. Wang and W. Zhang, *Synth. Met.*, 2013, **177**, 89–93.
10 T. K. Gupta, B. P. Singh, S. R. Dhakate, V. N. Singh and R. B. Mathur, *J. Mater. Chem. A*, 2013, **1**, 9138–9149.
11 Y. J. Chen, Z. Y. Lei, H. Y. Wu, C. L. Zhu, P. Gao, Q. Y. Ouyang, L. H. Qi and W. Qin, *Mater. Res. Bull.*, 2013, **48**, 3362–3366.
12 C. B. Cheng, K. L. Yan, R. H. Fan, L. Qian, Z. D. Zhang and K. Sun, *Carbon*, 2016, **96**, 678–684.
13 J. Liu, W. Q. Cao, H. B. Jin, J. Yuan, D. Q. Zhang and M. S. Cao, *J. Mater. Chem. C*, 2015, **3**, 4670–4677.
14 P. B. Liu, Y. Huang, L. Wang, M. Zong and W. Zhang, *Mater. Lett.*, 2013, **107**, 166–169.
15 M. Arjmand, M. Mahmoodi, G. A. Gelves, S. Park and U. Sundararaj, *Carbon*, 2011, **49**, 3430–3440.

16 C. Basavaraja, W. J. Kim, Y. D. Kim and D. S. Huh, *Mater. Lett.*, 2011, **65**, 3120–3123.

17 N. L. Yang, J. Zhai, M. X. Wan, D. Wang and L. Jiang, *Synth. Met.*, 2010, **160**, 1617–1622.

18 Y. Q. Yang, S. H. Qi, X. X. Zhang and Y. C. Qin, *Mater. Lett.*, 2012, **66**, 229–232.

19 M. H. Al-Saleh and U. Sundararaj, *Carbon*, 2009, **47**, 1738–1746.

20 M. S. Cao, W. L. Song, Z. L. Hou, B. Wen and J. Yuan, *Carbon*, 2010, **48**, 788–796.

21 R. Kumar, S. R. Dhakate, P. Saini and R. B. Mathur, *RSC Adv.*, 2013, **3**, 4145–4151.

22 V. K. Singh, A. Shukla, M. K. Patra, L. Saini, R. K. Jani, S. R. Vadera and N. Kumar, *Carbon*, 2012, **50**, 2202–2208.

23 O. C. Compton and S. T. Nguyen, *Small*, 2010, **6**, 711–723.

24 H. B. Zhao, Z. B. Fu, H. B. Chen, M. L. Zhong and C. Y. Wang, *ACS Appl. Mater. Interfaces*, 2016, **8**, 1468–1477.

25 J. H. Luo, Y. Xu, W. Yao, C. F. Jiang and J. G. Xu, *Compos. Sci. Technol.*, 2015, **117**, 315–321.

26 M. Zong, Y. Huang, H. W. Wu, Y. Zhao, P. B. Liu and L. Wang, *Mater. Lett.*, 2013, **109**, 112–115.

27 E. Ma, J. J. Li, N. Q. Zhao, E. Z. Liu, C. N. He and C. S. Shi, *Mater. Lett.*, 2013, **91**, 209–212.

28 M. Zong, Y. Huang, H. W. Wu, Y. Zhao, Q. F. Wang and X. Sun, *Mater. Lett.*, 2014, **114**, 52–55.

29 M. Zong, Y. Huang, Y. Zhao, L. Wang, P. B. Liu, Y. Wang and Q. F. Wang, *Mater. Lett.*, 2013, **106**, 22–25.

30 D. Sun, Q. Zou, G. Qian, C. Sun, W. Jiang and F. Li, *Acta Mater.*, 2013, **61**, 5829–5834.

31 K. Singh, A. Ohlan, V. H. Pham, B. R. S. Varshney, J. Jang, S. H. Hur, W. M. Choi, M. Kumar, S. K. Dhawan, B. S. Kong and J. S. Chung, *Nanoscale*, 2013, **5**, 2411–2420.

32 L. Wang, Y. Huang, X. Ding, P. Liu and M. Zong, *RSC Adv.*, 2013, **3**, 23290–23295.

33 P. Wu, N. Du, H. Zhang, C. Zhai and D. Yang, *ACS Appl. Mater. Interfaces*, 2011, **3**, 1946–1952.

34 Z. Liu, L. Phua, Y. Liu and C. Ong, *J. Appl. Phys.*, 2006, **100**, 093902.

35 X. W. D. Lou, L. A. Archer and Z. Yang, *Adv. Mater.*, 2008, **20**, 3987–4019.

36 L. Wu, H. Feng, M. Liu, K. Zhang and J. Li, *Nanoscale*, 2013, **5**, 10839–10843.

37 J. S. Chen, Z. Wang, X. C. Dong, P. Chen and X. W. D. Lou, *Nanoscale*, 2011, **3**, 2158–2161.

38 S. Pei and H. M. Cheng, *Carbon*, 2012, **50**, 3210–3228.

39 Y. Huang, Q. Cao, Z. Li, H. Jiang, Y. Wang and G. Li, *J. Am. Ceram. Soc.*, 2009, **92**, 2129–2131.

40 X. Yin, L. Kong, L. Zhang, L. Cheng, N. Travitzky and P. Greil, *Int. Mater. Rev.*, 2014, **59**, 326–355.

41 P. P. Kuzhir, A. G. Paddubskaya, M. V. Shuba, S. A. Maksimenko, A. Celzard, V. Fierro, G. Amaral-Labat, A. Pizzi, G. Valusis and J. Macutkevic, *J. Nanophotonics*, 2012, **6**, 066175.

42 X. H. Li, J. Feng, Y. P. Du, J. T. Bai, H. M. Fan and H. L. Zhang, *J. Mater. Chem. A*, 2015, **3**, 5535–5546.

43 J. H. Luo, Y. Xu, W. Yao, C. F. Jiang and J. G. Xu, *Compos. Sci. Technol.*, 2015, **117**, 315–321.

44 L. Zhang, X. H. Zhang, G. J. Zhang, Z. Zhang, S. Liu and P. F. Li, *RSC Adv.*, 2015, **5**, 10197–10203.

45 J. C. Wang, H. Zhou, J. D. Zhuang and Q. Liu, *Phys. Chem. Chem. Phys.*, 2015, **17**, 3802–3812.

46 L. Wang, Y. Huang, C. Li, J. J. Chen and X. Sun, *Phys. Chem. Chem. Phys.*, 2015, **17**, 2228–2234.

47 S. C. Zhao, Z. Gao, C. Q. Chen, G. Z. Wang, B. Zhang and Y. Chen, *Carbon*, 2016, **98**, 196–203.

48 L. Keller, K. Zahouily and S. Benfarhi, *Polymer*, 2005, **46**, 6640–6648.

49 Y. H. Han, A. Taylor, M. D. Mantle and K. M. Knowles, *J. Sol-Gel Sci. Technol.*, 2007, **43**, 111–123, mailto: kmk10@cam.ac.uk.

50 F. Bauer, R. Flyunt, K. Czihal, H. Langguth, R. Mehnert, R. Schubert and M. R. Buchmeiser, *Prog. Org. Coat.*, 2007, **60**, 121–126.

51 W. S. Hummers and R. E. Offeman, *J. Am. Chem. Soc.*, 1958, 801339.

52 J. J. Tang, J. Yang, X. Y. Zhou, H. M. Yao and L. M. Zhou, *J. Mater. Chem. A*, 2015, **3**, 23844–23851.

53 Z. Zhang, J. Bao, C. He, Y. N. Chen, J. P. Wei and Z. Zhou, *Adv. Funct. Mater.*, 2014, **24**, 6826–6833.

54 S. Dutta, A. Bhaumik and K. C. Wu, *Science*, 2014, **7**, 3574–3592.

55 M. Chen, X. W. Yin, M. Li, L. Q. Chen, L. F. Cheng and L. T. Zhang, *Ceram. Int.*, 2015, **41**, 2467–2475.

56 H. J. Yang, W. Q. Cao, D. Q. Zhang, T. J. Su, H. L. Shi and W. Z. Wang, *ACS Appl. Mater. Interfaces*, 2015, **7**, 7073–7077.

57 X. W. Yin, L. Kong, L. T. Zhang, L. F. Cheng, N. Travitzky and P. Greil, *Int. Mater. Rev.*, 2014, **59**, 326–355.

58 W. Y. Duan, X. W. Yin, F. X. Cao, Y. L. Jia, Y. Xie and P. Greil, *Mater. Lett.*, 2015, **159**, 257–260.

59 F. Ye, L. T. Zhang, X. W. Yin, X. F. Liu, Y. S. Liu, J. M. Xue, et al., *Mater. Lett.*, 2013, **111**, 169–172.

60 X. Y. Yuan, L. F. Cheng, L. Kong, X. W. Yin and L. T. Zhang, *J. Alloys Compd.*, 2014, **596**, 132–139.

61 X. F. Liu, L. T. Zhang, X. W. Yin, F. Ye, Y. S. Liu and L. F. Cheng, *Ceram. Int.*, 2015, **41**, 11372–11378.

62 X. M. Liu, X. W. Yin, L. Kong, Q. Li, Y. Liu and W. Y. Duan, *Carbon*, 2014, **68**, 501–510.